A Journal of the Gesellschaft Deutscher Chemiker

Angewandte International Edition GDCh Chemie

www.angewandte.org

Accepted Article

Title: Local structure of glassy lithium phosphorus oxynitride thin films: a combined experimental and ab initio approach

Authors: Maxwell A.T. Marple, Thomas A Wynn, Diyi Cheng, Ryosuke Shimizu, Harris Mason, and Ying Shirley Meng

To be cited as: *Angew. Chem. Int. Ed.* 10.1002/anie.202009501

Link to VoR: https://doi.org/10.1002/anie.202009501

WILEY-VCH

10.1002/anie.202009501

WILEY-VCH

RESEARCH ARTICLE

Local structure of glassy lithium phosphorus oxynitride thin films: a combined experimental and *ab initio* approach

Maxwell A.T. Marple*,+[a], Thomas A. Wynn+[b], Diyi Cheng[c], Ryosuke Shimizu[b], Harris E. Mason[a], and Y. Shirley Meng*[b],[c],[d]

[a] M.A.T. Marple, H. E. Mason
Physical and Life Science Directorate
Lawrence Livermore National Laboratory
Livermore, CA 94550, United States
E-mail: marple1@llnl.gov

[b] T.A. Wynn, R. Shimizu, Prof. Y. S. Meng
Department Department of NanoEngineering,
University of California San Diego

[c] D. Cheng, Prof. Y. S. Meng
Materials Science & Engineering Program
University of California San Diego

[d] Prof. Y. S. Meng
Sustainable Power and Energy Center
University of California San Diego
La Jolla, CA 92093, United States
E-mail: shirleymeng@ucsd.edu

+Contributed equally

Supporting information for this article is given via a link at the end of the document.

Abstract: Lithium phosphorus oxynitride (LiPON) is an amorphous solid-state lithium ion conductor displaying exemplary cyclability against lithium metal anodes. There is no definitive explanation for this stability due to the limited understanding of the structure of LiPON. We provide a structural model of RF-sputtered LiPON via experimental and computational spectroscopic methods. Information about the short-range structure results from 1D and 2D solid-state nuclear magnetic resonance experiments investigating chemical shift anisotropy and dipolar interactions. These results are compared with first principles chemical shielding calculations of Li-P-O/N crystals and *ab initio* molecular dynamics-generated amorphous LiPON models to unequivocally identify the glassy structure as primarily isolated phosphate monomers with N incorporated in both apical and as bridging sites in phosphate dimers. Structural results suggest LiPON's stability is a result of its glassy character. Free-standing LiPON films are produced that exhibit a high degree of flexibility highlighting the unique mechanical properties of glassy materials.

Introduction

Solid-state lithium ion conductors are attractive electrolytes for next generation lithium ion batteries due to their improved safety and their potential to improve energy density by enabling the use of lithium metal anodes.[1] However, in practice the use of Li metal anodes is hindered by electrolyte decomposition and the formation of high impedance interfaces[2] or the formation of Li dendrites.[3] This degradation diminishes coulombic efficiency and Li dendrite formation causes catastrophic failure via cell shorting. A fundamental understanding of solid electrolytes relative stability against Li metal is required to surmount the issue of degradation; however, the relevant properties leading to stability is currently disputed. Standard descriptions of the electrochemical stability window of solid-state interfaces rely on calculations of the grand potential phase diagrams to compute interface stability, drawing parallels to the solid electrolyte interphase in liquid electrolytes.[2,4] However, mechanisms of electrochemical decomposition are incomplete, and generally do not incorporate kinetics into these models, with recent exceptions.[5]

While many material properties of crystalline compounds can be predicted by thermodynamic calculations, the same is not true for glassy materials as they are non-equilibrium and their formation and properties are largely driven by kinetics. Traditionally a glass is formed after atomic motion is kinetically arrested during the rapid quench from a melt. The configurational state that is frozen is a local potential energy minimum within a potential energy landscape. The subsequent thermodynamic properties of the glass are dictated by the local potential energy minima and transitions between these minima govern the relaxation and transport kinetics.[6] The glass is metastable as the kinetics for crystallization or decomposition become impossibly slow on any reasonable, 'human' time scale. As kinetics are paramount to glass properties, by not considering kinetics in electrochemical decomposition models the response of glassy solid electrolytes will be incorrect. Notably, glassy solid electrolytes are of interest because they lack grain boundaries that can be sources of electrostatic and structural inhomogeneities[7] and charge transfer impedance,[8] and they can have wider compositional stability than analogous crystals so they may tolerate ionic depletion and not undergo a phase transformation.[9] However, glassy electrolytes such as lithium phosphorus oxynitride (LiPON) and lithium thiophoshates are both experimentally and computationally challenging to investigate: experimentally, methods for explicit

structural determination are limited; computationally, disordered solids are more difficult given the prevalence of periodic boundary conditions in most theory. LiPON electrolytes, which have a composition of $Li_xPO_yN_z$, where x = 2y + 3z − 5, were pioneered at Oak Ridge National Laboratory.[10] Most often attained by RF sputtering Li_3PO_4 in a N plasma, LiPON is particularly interesting due to its remarkable cyclability against lithium metal—a crucial requirement for next-generation lithium ion batteries.[11] LiPON's stability has been attributed to a number of features: low electronic conductivity (10^{-15}-10^{-12} S cm^{-1})[3], mechanical rigidity[12], formation of electrically insulating and ionically conducting decomposition products, Li_3P, Li_3N, Li_2O, supported by density functional theory (DFT) predictions and *in situ* x-ray photoelectron spectroscopy *(*XPS)[2,13,14], and kinetic stability of those interfacial components.[15]

Despite the exemplary electrochemical stability LiPON displays, there is a pervasive lack of understanding and inconsistency in describing the local structure of LiPON. Many of these comments are already discussed elsewhere with much of the confusion stemming from how N is incorporated into the structure and the types of local structural units.[16,17] These issues arise from observations made on metaphosphate oxynitride glasses where XPS results indicated N crosslinks the network by bonding to three and two P tetrahedra denoted N_t and N_d, respectively. Others claim structural models of LiPON include extended chain structures where many P tetrahedra are linked by bridging O or N similar to metaphosphate glasses or even a layered structure of Li and P rich regions.[10,14,18–20] These descriptions are inconsistent with the structure of LiPON's precursor orthophosphate material Li_3PO_4 that is composed of isolated P tetrahedra. As a result, existing kinetic models for the Li/LiPON interfaces overestimate structural instability through an overabundance of such metastable coordination environments.[15,19] In this regard, accurate local structural descriptions are of utmost importance in describing the chemical environments leading to the enhanced stability. Recent investigations have shown through a combination of neutron scattering and *ab initio* molecular dynamics (AIMD) that N is incorporated into LiPON by forming both dimeric $P_2O_6N^{5-}$ units where N is bridging (N_d) and a non-bridging N site on isolated PO_3N^{4-} units (apical N, N_a).[16,21] They find no evidence of N_t and offer alternative assignments for XPS and IR spectroscopic results in support of their findings.

Solid-state nuclear magnetic resonance (NMR) spectroscopy is particularly suited for the determination of structure in glasses as it is sensitive to short range order and can probe a number of interactions like chemical shift anisotropy (CSA), dipolar and quadrupolar coupling that contain unique information to help distinguish different chemical environments within an amorphous material. Notably it offers quantitative insight into the constituent short range structural units of LiPON and can validate recently proposed structural models.[22] The typical connectivity nomenclature for phosphate glasses is given by the number of bridging oxygens (BO) per tetrahedral P atom, Q^n, where *n* is the number of bridging atoms and ranges from 3 to 0. A network composed of Q^3 units is three dimensional, whereas a Q^2 network is defined by chains, Q^1 network is composed solely of dimeric units, and Q^0 by isolated PO_4^{3-} tetrahedra.[23] Modifying cations like Li act to depolymerize the network by forming non-bridging oxygen (NBO) atoms randomly throughout the network, thus direct insight into the network connectivity is gained by tracking the population of the Q units, and the Q^n speciation corresponds directly to the Li:P ratio. To account for the mixed-anion effect on connectivity we introduce a modification of the Q^n nomenclature, Q^n_m where *m* is the number of non-oxygen anions on the P tetrahedra and can take on values between 0 to 4. In the case of LiPON, *m* indicates the number of nitrogen atoms per P tetrahedra as N substitutes O when it is incorporated into the glass network.[24] Other NMR investigations have been performed on LiPON, however these studies focused on LiPON synthesized by atypical deposition methods and on bulk LiPON glasses closer to metaphosphate compositions.[25,26] In this work, we employ advanced 2D NMR techniques to differentiate the local chemical shift anisotropic features and dipolar interactions permitting structural determination to resolve the local structure of RF-sputtered LiPON. The experimental NMR results are compared to those from density functional theory using the gauge including projector augmented wave (GIPAW) framework to calculate the chemical shieldings of a variety of lithium phosphorus oxynitride crystals, developing a database of local bonding environments and their corresponding chemical shielding. These calculated shielding values and CSA parameters are compared to the measured chemical shifts from NMR measurements, and are then used to validate AIMD-amorphized LiPON structure. This combined experimental and computational study provides unique information of the local structure and is consistent with recently proposed structural models, thus providing a definitive and unequivocal local structural model of LiPON.[16,21] Such structural validation is crucial for developing an atomic level understanding of the electrochemical stability of this electrolyte when paired with lithium metal.

Results and Discussion

^{31}P MAS NMR of LiPON

NMR is sensitive to short range structure, making it an invaluable tool for structural identification of glasses wherein the connectivity of structural units is resolved as separate chemical shifts. For investigating structure, ^{31}P NMR is favorable as it is a sensitive nucleus to local chemical environments and is a 100% abundant. The deconvolution and subsequent interpretation of the ^{31}P spectra of LiPON is non-trivial and requires the simultaneous consideration of the experimental and calculated results to create a consistent structural model. The ^{31}P magic angle spinning (MAS) spectrum of LiPON (Fig. 1) shows a broad peak centered at 10 ppm with a high frequency shoulder. The line shape is broadened by structural disorder arising from a distribution of bond lengths and angles and consequently a chemical shift distribution.

To aid in interpreting the ^{31}P line shape of LiPON, spectra of the target material, crystalline β-Li_3PO_4 (c-LPO), and RF-sputtered amorphous films of Li_3PO_4 (a-LPO) are collected (Fig. S3). The ^{31}P chemical shift for c-LPO has a sharp peak at 9.6 ppm in accordance with orthophosphate tetrahedra having four non-bridging oxygen, Q^0. After amorphization, a-LPO shows a broadening of the Q^0 peak indicating structural disorder. A shoulder is observable at ~0 ppm that can be attributed to dimeric P_2O_7 units, Q^1, suggesting about 3 mol% Li_2O is lost during the sputtering process, as alkali phosphate glasses follow a random

10.1002/anie.202009501

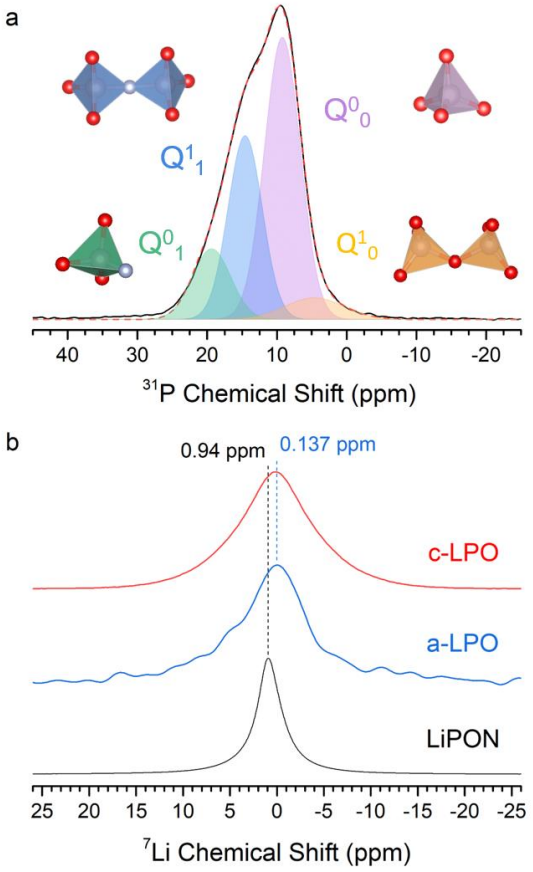

Figure 1. (a) ^{31}P MAS NMR spectra of free-standing thin film LiPON spinning at 25 kHz, (b) ^{7}Li MAS NMR spectra of powder Li_3PO_4, thin film amorphous Li_3PO_4, and free-standing thin film LiPON.

binary distribution in terms of Q speciation with cation concentration.[27] The chemical shift for Q^1 is slightly higher than observed in a pyrophosphate crystal[28], likely a result of a redistribution of the electron density with higher cation concentration. Increases of up to 10 ppm for a Q^n species with increasing cation concentration have been previously observed.[29] The MAS ^{31}P spectrum of a LiPON film (Figure 1a) bears resemblance to the a-LPO spectra with the predominant intensity at 9.1 ppm and a small tail around 3 ppm; these sites can be comfortably assigned to Q^0_0 and Q^1_0 phosphate species, respectively. However, in contrast to the a-LPO film, there are additional shoulders to higher chemical shift that are presumed to be phosphorus bonded to N. Further assignments are hindered by a lack of understanding of how N is incorporated into alkali pyro- and orthophosphate glasses due to the spontaneous crystallization upon quenching during synthesis, prohibiting further investigation. Previous studies on the effect of nitridation in metaphosphate glasses have found a similar rise of higher frequency peaks that are attributed to forming various PO_3N and PO_2N_2 Q^n_m units.[26,30,31]

We turn to first principles calculations of a database of lithium phosphorus oxynitride compounds (Tables S4-S7) and AIMD simulations of LiPON (Table 1, SI) to aid our assignments. These methods are discussed in the following section and detailed in Supplementary Information (SI). Our results indicate the ^{31}P spectra of LiPON (Fig. 1) can be deconvoluted into 4 peaks, the majority of which is composed of Q^0_0 PO_4^{3-} units at 9.3 ppm, followed by Q^1_1 $P_2O_6N^{5-}$ dimer units in which N is bridging two PO_3N tetrahedra whose δ_{iso}=14.6 ppm; the other nitride species at 19.4 ppm is assigned to Q^0_1 PO_3N^{4-} units, and a minor amount of Q^1_0 $P_2O_7^{4-}$ dimers as previously mentioned. These assignments give important insight into how N is incorporated into the LPO network, suggesting that N acts similarly to O, as both a bridging (as observed in the Q^1_1 site) and non-bridging (the Q^0_1 site) anion. The overall line shape is similar to that of previously published ^{31}P NMR of IBAD deposited LiPON, with similar peak positions and broadening that is associated with N incorporation.[25] However, the IBAD spectrum shows diminished intensity above 12 ppm in comparison, indicating the network has less Q^1_1 and no Q^0_1 units. The observation of entrapped N_2 gas within the IBAD film agrees with this finding that less N is incorporated with the IBAD process.

While ^{31}P NMR offers insight into the network structure, ^{6}Li (Figure S4) and ^{7}Li (Figure 1b) chemical shifts of c/a-LPO and LiPON were collected to understand the changes of the Li environments. Both ^{6}Li and ^{7}Li chemical shifts of LiPON increase by ~1 ppm relative to c-LPO and a-LPO as a result of the lowering Li coordination to less than 4.[22] The ^{7}Li line shape of LiPON is narrowed relative to a/c-LPO suggesting increased Li conductivity, in agreement with dielectric spectroscopy measurements.[32] It should be noted, the ^{7}Li LiPON line shape has a Lorentzian character indicating the Li ions are mobile at room temperature and rapidly exchanging between sites, hence a single peak is observed.

Computational spectroscopy of lithium oxynitride phosphates

To accurately correlate NMR chemical shifts with local structures and remove ambiguity in the assignments of chemical environments, we employ DFT calculations to simulate the effective electronic shielding of a variety of relevant lithium phosphorus oxynitride compounds. Recent implementation of the GIPAW approach has enabled precise determination of electronic shielding effects on nuclei in solids[33,34] that directly relate to chemical shifts determined via NMR measurements.[35] The chemical shielding is related to chemical shift by a correlation factor based on experimentally determined chemical shifts (SI). With this correlation factor, isotropic chemical shifts, δ_{iso}, and CSA parameters can be calculated for all the structures in the database allowing for systematic trends of the structures with chemical shift to be observed. The VASP implementation of the GIPAW approach was applied to a body of lithium phosphorus oxynitride crystals of varied compositions and bonding environments; the list of compounds and their calculated chemical shifts are shown in Tables S4-S7. To confirm prediction of known structural groups, calculations were performed for Li_3PO_4 (Q^0 PO_4), $Li_4P_2O_7$ (Q^1 PO_4 dimers), and $LiPO_3$ (Q^2 PO_4 chains), along with some phosphorus nitride and oxynitride variants, shown in Figure 2; corrected δ_{iso} (Figure S12) are accurately predicted in comparison to experimentally determined isotropic chemical shifts and tensor elements (Table S5 and S8). By organizing all the compounds in the database by their Q^n speciation and anion type (Fig. 2b, left), there is a clear trend showing that as Q^n is reduced the ^{31}P chemical shift correspondingly increases by about 16-20 ppm. This agrees with previous observations of Q^n speciation trends in phosphate glasses[36] and shows that the Q^n speciation largely

10.1002/anie.202009501

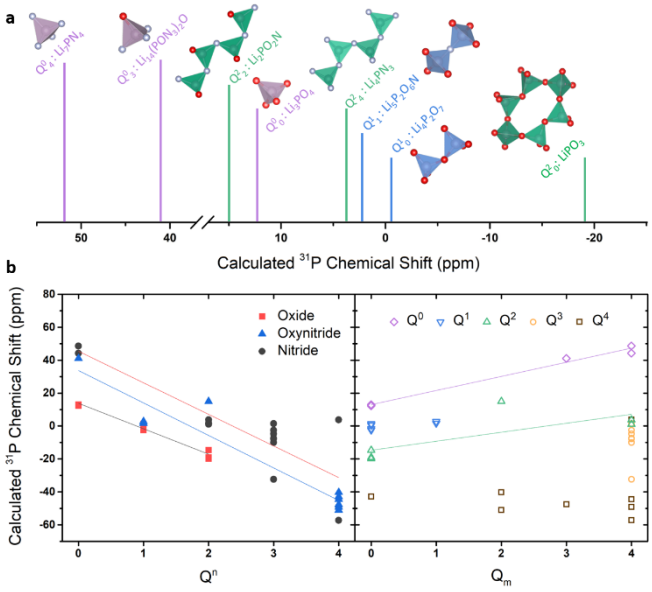

Figure 2. (a) Calculated isotropic ^{31}P chemical shifts of representative Q^n_m structures to illustrate chemical shift variation with Q speciation. (b) Calculated isotropic ^{31}P chemical shift variation with Q^n (left) and Q_m (right) to reveal the effect of network connectivity and N incorporation, respectively.

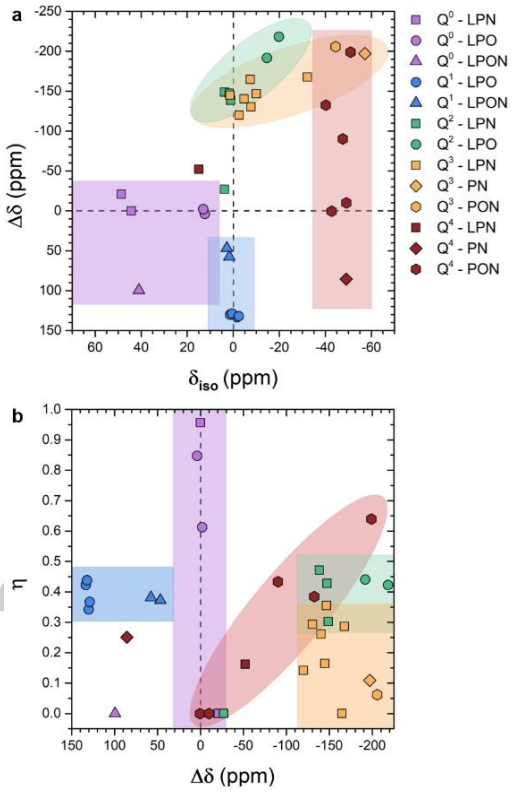

Figure 3. Calculated (a) anisotropy-isotropic chemical shift and (b) anisotropy-asymmetry correlation maps of the GIPAW database compounds grouped by Q^n_m speciation showing distinct ranges.

dictates δ_{iso}. While the database lacks many representative data points, the effect of nitridation has a clear effect on δ_{iso} although weaker in comparison to the effect of Q^n. As the variation of δ_{iso} of the Q^0_m units shows, δ_{iso} increases with increasing nitridation (Q_m) by about 10 ppm for every N replacing O, and likely applies to all Q^n species. This trend agrees with previous studies investigating the effect of nitridation of phosphate glasses that found N has a deshielding effect on ^{31}P when replacing O as it has less electronegativity.[26,30,37,38]

A few structures deviate from these δ_{iso} trends, such as $Li_5P_2O_6N$, where all Q^1_1 units with bridging N is much lower (δ_{iso}=~2 ppm) than the chemical shift for Q^1_1 units (δ_{iso}= 14 ppm) found in LiPON. This is due to the strong dependence of the P-N-P bond angle with chemical shift, likely a shielding effect from overlapping terminal P=O bonds that are much weaker in LiPON (SI). The database includes the only two compounds with N_t environments (P_3N_5 and P_4N_6O), having ^{31}P chemical shifts in the range -57 to -44 ppm, well outside the range observed for LiPON. Additionally, no ^{31}P chemical shift corresponding to Li_3P (δ_{iso}=-278 ppm) was observed in the MAS LiPON spectrum, indicating the intermetallic phase does not form as an impurity within or on the surface of the thin film. However, an unknown impurity phase is detected at 115 ppm that is tentatively assigned to three coordinated P defect sites at the surface (SI).

As Fig. 2 shows, many Q^n_m units have isotropic chemical shifts in the range found for LiPON (20-0 ppm), thus comparison of isotropic chemical shifts alone cannot be used for definitive assignments. However, the GIPAW computational method calculates the full chemical shift tensor, which translates to the chemical shift anisotropy (CSA). The CSA reflects the distortion of the electronic structure around the nucleus and contains information regarding the local symmetry of said nucleus, which is fully described by two parameters, anisotropy Δδ and asymmetry η (see SI for full convention definition). The chemical shift tensor elements are also included (Table S5 and S8) to verify the accuracy of the CSA parameters and mitigate the assignment error that the Haeberlen convention is prone to (Δδ and η).[39] These CSA parameters provide distinction of different structures based on their local symmetry despite having similar chemical shifts. CSA analysis is especially useful for disordered structures as it provides the means to distinguish different chemical environments despite overlapping resonances.[36,40,41] The calculated δ_{iso} and CSA parameters are grouped by their corresponding Q^n_m speciation (Fig. 3) to reveal distinct clustering primarily by their Q^n designation. The Q^0_m units are all marked by negligible Δδ and η close to 1, reflecting the tetrahedral symmetry of isolated P tetrahedra. The Q^1_m units display moderate and positive Δδ values ranging from 50 to 120 ppm with η around 0.4, while the Q^2_m and Q^3_m units have negative and large Δδ values with η less than 0.4. These CSA differences are key to identifying and correctly assigning the resonances seen in LiPON at higher chemical shifts.

Computational spectroscopy of LiPON glass

AIMD was used to generate representative model structures from which the chemical shift tensors of the constituent local structural units can be calculated. As there are limited number of oxynitride crystals available, this method removes uncertainty of assignments in the composition gaps in the alkali phosphorus oxynitride variants. To both confirm application of the structural database to the amorphous structure demonstrated in LiPON, AIMD approach is employed to generate an amorphous structure with a stoichiometry of $Li_{2.9}PO_{3.5}N_{0.31}$, shown in Figure 4a.[16] Previous studies performed AIMD-based melt quenches on a

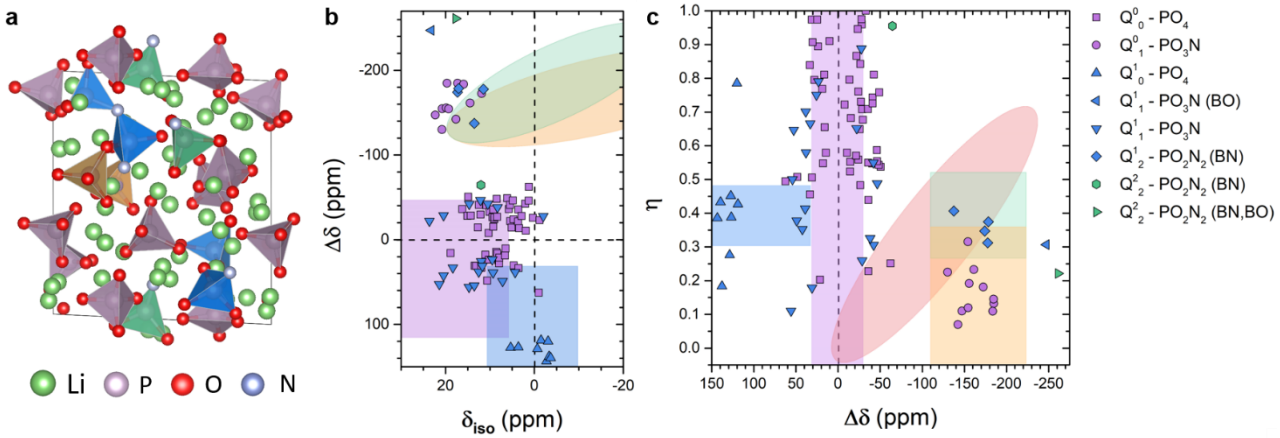

Figure 4. (a) Schematic AIMD model of LiPON. Coloration of the P tetrahedra correspond to the Q^n_m speciation. Q^0_0 purple, Q^1_1 blue, Q^0_1 green, Q^1_0 orange. (b) Anisotropy-isotropic chemical shift and (c) anisotropy-asymmetry correlation maps of the AIMD model grouped by Q^n_m speciation showing distinct ranges.

variety of LiPON stoichiometries, clearly linking the Li and N content to the potential for bridging configurations and subsequently improved ionic conductivity, σ_i, via modified coulombic interactions.[22] They also concluded the low density achieved through AIMD melt-quenching rules out previous interpretations of the opening of the structure to σ_i improvement, instead correlating decreased density to improved conductivity.[22] However, distinctions between classical metaphosphate glasses and vapor deposited glasses emphasize limitations of the melt-quench method for producing the high-density glasses attained through physical vapor deposition. To emulate the high density of a vapor deposited glass, NVT quenches with densities on the order of crystalline analogues were performed. The AIMD-determined structures are generally consistent with that previously reported, however, upon repeated melts and quenches of the structures of increased density, occasional variations in coordination are observed including the formation of a Q^2_2 units in a trimer chain, clearly emphasizing the propensity for N as a bridging unit; the low number of such structures suggests they would be difficult to detect with conventional solid-state NMR techniques.

Using this structure, GIPAW calculations are performed to calculate the relationship between bonding environment and electron shielding (Figure 4b,c). A range of δ_{iso} are present for the ^{31}P calculations, likely due to variation in Li coordinations and bond angles. Consistent with observations from the structural database, incorporation of N results in an increased δ_{iso}, whereas the lowest δ_{iso} is associated with bridging oxygen. While a projection of these datapoints mirror the experimental δ_{iso} range, calculations of the CSA parameters $\Delta\delta$ and η may clearly be used to deconvolute this clustering. For example, Q^1_0 units show a distinct $\Delta\delta$ >100 ppm. The average δ_{iso} and CSA parameters for the corresponding sites are listed in Table 1. The model predicts a structure that is dominated by Q^0_0 units followed by Q^1_1 and Q^0_1 units with minor amounts of Q^1_0 (Table 1) and indicates N incorporation prefers bridging over non-bridging sites. The model also predicts a singular Q^2_2 unit existing as the center tetrahedra in a trimer chain. Given the limited size of the unit cell and relatively small number of atoms, we do not consider these trimer units to be representative structural units in LiPON.

The crystal database and AIMD model provide important insight regarding the nature of N incorporation in LiPON and related compounds. Despite many claims, primarily spurred by XPS assignments stating N is coordinated to 3 P tetrahedra (N_t) to form a tricluster in LiPON, we find no evidence in the present study to support these assignments, consistent with previous findings using other techniques.[16,21,42] A detailed discussion on this topic with results from GIPAW calculations of ^{15}N chemical shifts is provided in the SI.

2D NMR spectroscopy of chemical shift anisotropies

As the 1D ^{31}P spectrum (Fig. 1) and the AIMD model (Fig. 4) reveal, there is significant overlap of the constituent Q^n_m δ_{iso} making deconvolution of the 1D MAS spectrum non-trivial. But as the CSA from the AIMD model shows, there are substantial differences between the CSA of the Q^n_m units, which permits identification of convoluted peaks. The MATPASS/CPMG pulse sequence is used to sequester the anisotropic components into

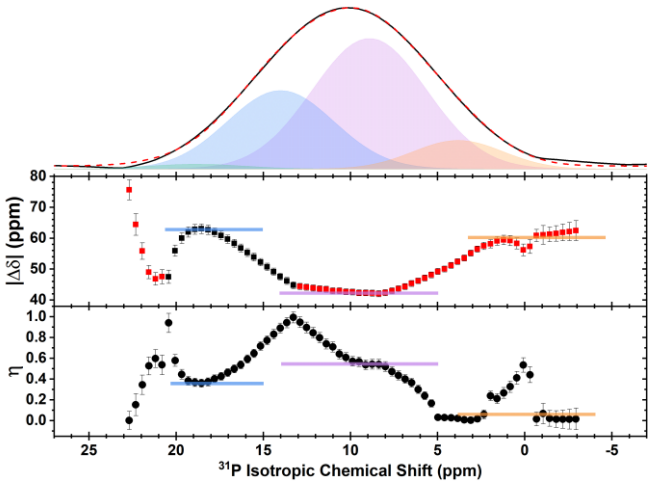

Figure 5. ^{31}P MATPASS (top) Isotropic projection with deconvolution informed by CSA parameter variation, colors are consistent with Fig. 1. (middle) Anisotropy and (bottom) asymmetry variation with isotropic chemical shift. Solid lines reflect the range where one component's CSA parameters are the dominant contribution.

Table 1. NMR parameters used for deconvolution of the 1D MAS ^{31}P spectrum of LiPON spinning at 25 kHz and the corresponding NMR parameters obtained from the AIMD model of LiPON.

Site	δ_{iso} (ppm)[a]	δ width (ppm)[a]	Δδ (ppm)[b]	η	Relative Fraction (%)
1D MAS					
Q^0_0	9.3	6.1	-37	0.67	49
Q^1_1	14.6	5.8	42	0.70	30
Q^0_1	19.4	6.5	-150	0.30	14
Q^1_0	4.7	10	-98	0.30	7
AIMD					
Q^0_0	7.82	4.55	29.7[b] ±12.8	0.67 ±0.19	53.1
Q^1_1	12.77	6.15	38.4[b] ±10.1	0.50 ±0.21	19.8
Q^0_1	18.15	2.96	-161 ± 17.6	0.17±0.07	11.5
Q^1_0	-0.75	3.19	130 ±8.5	0.42±0.16	8.3
Q^1_2	14.83	2.45	-166.9±17	0.36±0.03	4.2
Q^1_1	23.21	-	-247	0.31	1
Q^2_2	12.04	-	-64.5	0.96	1
Q^2_2	17.72	-	-261	0.22	1

[a] AIMD shift and width indicate the average and standard deviation of δ_{iso}, respectively. [b] Absolute value for Δδ used as an estimate of the magnitude of the CSA, otherwise underestimated due to sign variation.

a secondary dimension that can be modelled to extract the CSA parameters at each isotropic chemical shift (SI).[43] Additionally, the projection of the 2D experiment produces a spectrum that is free of CSA, having only isotropic contributions to the chemical shift (Fig. 5 top). The intensity above 20 ppm is not completely refocused due to rapid dephasing of the Q^0_1 units from short T_2 (see SI). It is evident the magnitude of Δδ does not vary much, as all measured values fall between 65 and 40 ppm. These anisotropy values are rather small and by comparison to some values in Fig. 3 rule out the presence of Q^2_m or Q^3_m units within LiPON. Rather, the small Δδ values indicate the Q^0_0 and Q^1_1 units dominate the structure as they tend to have smaller Δδ. In the case of the Q^0_0 units observed in the crystals Δδ is nearly zero, reflecting a symmetric site, whereas in LiPON it is reasonable to consider deviations from this local symmetry arising from a distribution of bond lengths hence the larger Δδ. The variations of Δδ and η with δ_{iso} display three regions where the values plateau (Fig. 5b, solid lines), indicating minimal overlap of multiple resonances and the predominance of a singular chemical environment. These plateaus correspond to three of the constituent Q^n_m units: Q^0_0 (δ_{iso} = 9 ppm) with Δδ= -42 and η=0.54, Q^1_1 (δ_{iso} =14) with Δδ=63 and η=0.36 , and Q^1_0 (δ_{iso} =3.8) with Δδ=-61 and η=0.06. It should be noted that η appears as 1.0 in the case of two superimposed sideband patterns with opposite signs of Δδ and explains rise of η at δ_{iso} = 13.2 and 20.4 ppm; these points are artifacts denoting overlapping regions and produce a gradual rise and fall with δ_{iso}. The gradual changes between the CSA parameters provide guidance on the peak width of their corresponding sites to aid in deconvolution of the MAS spectrum. One component not featured is the Q^0_1 peak at 19.4 ppm, as it has greatly lower intensity in comparison to the MAS spectra in Fig. 1. This absence is a result of the rapid dephasing occurring during the MATPASS pulse sequence at lower spinning speeds, making it unable to refocus this component. However, traditional side band analysis at various spinning speeds reveals the CSA of this site to be significantly larger than other sites (Δδ = -150 ppm and η = 0.3). The sideband analysis also provides CSA parameters of the other sites that are consistent with the results from MATPASS and the AIMD model. Overall, the MATPASS and sideband CSA analysis indicate there are four peaks: the Q^0_0 and Q^1_1 sites, having relatively small anisotropies, and the Q^0_1 and Q^1_0 sites, having much large anisotropies. MATPASS results and a comparison to the MAS sideband analysis is detailed in the supplementary information. The corresponding values agree with the calculated values from the AIMD model.

In conjunction with the CSA analysis, further insight into the chemical identity and connectivity of the local structure comes from double-quantum (DQ) build-up curves and DQ-SQ correlation spectroscopy (Figure S9). These DQ experiments (detailed in the SI) rely on probing the ^{31}P-^{31}P homonuclear dipolar coupling interaction and can reveal the connectivity of Q^n environments, potentially revealing details on extended chain environments.[44] The results from the buildup curves produce P-P interatomic distances in agreement with those from neutron scattering.[16] DQSQ correlation spectroscopy shows that all P environments are correlated with themselves and all other units indicating the Q^n_m units are randomly distributed through the network. The results also support the identification of the ^{31}P chemical shift at 19 ppm to the Q^0_1 unit. These results solidify there are no extended chain structures or layers within LiPON and indicate the network structure is dominated by isolated P tetrahedra and dimeric units.

The combined experimental and computational results reveal the structure of LiPON is composed of Q^0_0 (49%), Q^1_1 (30%), Q^0_1(14%), and Q^1_0 (7%) units, with assignments and isotropic chemical shifts informed by their CSA parameters and comparison to the AIMD model. As the ^{31}P NMR results were collected quantitatively, the 1D MAS deconvolution can be used to estimate the composition as a check for internal consistency of the assignments. This produces a composition of $Li_{2.93}PO_{3.52}N_{0.30}$, mirroring films of similar ionic conductivity. The AIMD model suggests there may be other minor structural units present making up 1% of the P units, though these are all too low in concentration to observe experimentally and are omitted from the deconvolution. The Q^1_2 unit is in slightly higher concentration (~4%) though its δ_{iso} is expected to be close to the Q^1_1 unit and cannot be fully resolved in the spectra; its contribution is included into the Q^1_1 peak. Although if this contribution is included separately and makes up to 4% of the P environments a marginally closer estimate of the composition is obtained. Additionally, the deconvolution allows us to indirectly determine the quantity of N_d and N_a, as the N_a are exclusively associated with Q^0_1 units and all N_d are forming dimers in the Q^1_1 units. From our NMR assignments and fit we obtain 67% N_d and 33% N_a. These values are entirely consistent with the results obtained by Lacivita et al. who found the N_d:N_a ratio depends on the Li:O+N ratio, predicting 60% N_d and 40% N_a for our composition.[16] The internal consistency and agreement of our assignments with other experimental and modelling results indicate our assignments and

deconvolution accurately represent the structure of RF sputtered LiPON.

A Glassy Perspective of LiPON

Understanding the structure of LiPON is essential for determining its electrochemical properties. The general trend for lithium phosphorus oxynitride glasses is with higher Li content the conductivity concomitantly increases, as expected from σ_i=neμ. However, at high Li content, N incorporation is shown to enhance the mobility through formation of dimers with bridging N which attract Li less strongly than PO bonds.[16,22] There is a limit however, as increasing Li relative to N breaks the N_d to form non-bridging N, that have a stronger interaction with Li and consequently lowers conductivity. The structural assignments developed here indicate ^{31}P NMR can be used as an indirect measure of the N_a to N_d ratio in LiPON related materials. The introduction of N into the network however does not necessarily provide any indication as to why LiPON is so stable against Li metal.

Considering LiPON is a glassy material, we advocate a possible theory for LiPON's stability that relies on its glassy nature.[45] In accordance to the ultra-stable glasses investigated by Ediger et al., physical vapor deposited (PVD) glasses show remarkably low fictive temperatures indicating they are close to the bottom of their potential energy landscapes, resulting in kinetic and chemical stabilities that cannot be achieved by conventional heat treatments on reasonable timescales.[46,47] This enhanced kinetic stability has been observed in PVD organic[48], metallic[49], and chalcogenide[50] glasses and considering LiPON is grown by a form of PVD, it is reasonable to assume it too can display a low fictive temperature after deposition. The implication of LiPON as a low fictive temperature glass is that it is nearing the bottom of its potential energy landscape thus the energy difference between the metastable glassy state and the corresponding crystalline state is minute.[51] This minimizes the thermodynamic driving force for crystallization and the enthalpy barriers for initiating structural rearrangement are too high to overcome on an experimental timescale and are consequently suppressed. This enhanced kinetic stability observed in ultra-stable glasses could be a possible explanation for the superior electrochemical stability LiPON presents with Li metal. Even with the interfacial driving force to decompose, the kinetic stability of LiPON in its 'stable' form may reduce the decomposition rate. This also implies that

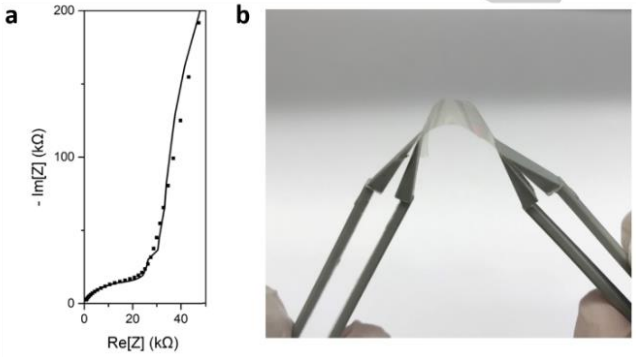

Figure 6. A 3.75 μm thick free-standing film of LiPON is produced, showing (a) ionic conductivity similar to its confined film counterparts (σ_i = 2.6 μS/cm) and (b) a remarkable degree of film compliance.

LiPON's stability may not be only related to the chemistry of LiPON but also a consequence of the unique synthesis route in which it is made. How ultra-stable glass kinetic stability relates to electrochemical stability remains to be seen and requires further studies explicitly investigating the connection. Previous work has explored the increased kinetic stabilization of LiPON via annealing at a variety of temperatures below the measured T_g of bulk counterparts. Among their results, annealing temperature was shown to have little effect on composition, attributing all conductivity changes to structural and configurational modifications, albeit in 50 nm thick films.[52] While deposition is not controlled in these experiments, literature has reported an increase in temperature up to 110°C due to plasma heating of the film during deposition.[53] Such surface heating enhances mobility of surface ions, resulting in increased glass density.[48] However, this is below the critical annealing temperature before a severe drop of ionic conductivity is observed (~150ºC).[45] The potential for plasma heating is one further variable among the LiPON deposition field, and likely accounts for variable performance and stability.

Last, sources of the high degree of cyclability of Li/LiPON cells likely extend beyond electrochemical stability of LiPON itself. Mechanically, the lack of connectivity coupled with the high cation concentration appears to manifest a high degree of film compliance. As the structure is dominated by Q^0_0 and Q^1_1 units with N acting to bridge about 30% of the phosphate tetrahedra as dimeric units, the overall LiPON network structure clearly does not contain any extended chain structures as indicated by DQSQ results and absence of CSA values expected for Q^2 environments. Interestingly, the free-standing films of LiPON produced for this study exhibit a high degree of flexibility considering the film thickness (Figure 6b). This degree of compliance is surprising, and questions current requisites for a solid state electrolyte to resist dendrite penetration, generally purported to require a critical modulus.[54] Such flexibility is commonly observed in chemically-tempered alkali-aluminosilicate glasses, where fracture is prevented by a lack of surface defects. The flexibility in LiPON glass suggests that the presence of undercoordinated P groups (see SI) do not behave as defects, or as a detriment to the film's mechanical properties. Such flexibility is likely enhanced by using PVD processes, which produces smooth, uniform films. This mechanical compliance will be explored in future work.

Conclusion

Using 1D and 2D solid-state NMR methodologies, the local structure of amorphous LiPON is definitively resolved, showing the prevalence of Q^0_0 tetrahedra and identifying N incorporation to form dimeric units via bridging N and separately non-bridging N on orthophosphate tetrahedra. GIPAW methodologies permit calculation of a range of phosphate-based compounds, clearly identifying trends in chemical shift tensors as a function of composition and local structure. Experimentally measured chemical shift anisotropy parameters of LiPON are accurately assigned, guided by calculated chemical shielding tensor elements of AIMD generated LiPON structures and relevant lithium phosphorus oxynitride crystal structures. The high stability of LiPON is described structurally as a combination of the low connectivity of the structure as well as the hyperannealing that occurs with physical vapor deposition. Free-standing films of

LiPON are produced, exhibiting a high degree of flexibility, and hence compliance, which further supports the lack of long-range order and questions the role of mechanical properties in the cyclability of LiPON.

Acknowledgements

The authors gratefully acknowledge funding support from the U.S. Department of Energy, Office of Basic Energy Sciences, under Award Number DE-SC0002357 (program manager Dr. Jane Zhu). XPS work was performed at the UC Irvine Materials Research Institute (IMRI) using instrumentation funded in part by the National Science Foundation Major Research Instrumentation Program under grant no. CHE-1338173. This work also used the Extreme Science and Engineering Discovery Environment (XSEDE), which is supported by National Science Foundation grant number ACI-1548562. This work was performed under the auspices of the US Department of Energy by LLNL under contract number DE-AC52-07NA27344. The project was supported by Laboratory Directed Research and Development (LDRD) program of LLNL, award number 20-FS-012. LLNL tracking number: LLNL-JRNL-810272.

Keywords: Solid-State NMR • Ab initio calculations • Solid Electrolyte • GIPAW • LiPON

1 Q. Zhao, S. Stalin, C. Z. Zhao and L. A. Archer, *Nat. Rev. Mater.*, 2020, 5, 229–252.
2 W. D. Richards, L. J. Miara, Y. Wang, J. C. Kim and G. Ceder, *Chem. Mater.*, 2016, **28**, 266–273.
3 F. Han, A. S. Westover, J. Yue, X. Fan, F. Wang, M. Chi, D. N. Leonard, N. J. Dudney, H. Wang and C. Wang, *Nat. Energy*, 2019, **4**, 187–196.
4 Y. Zhu, X. He and Y. Mo, *J. Mater. Chem. A*, 2015, **4**, 1–14.
5 H. Tang, Z. Deng, Z. Lin, Z. Wang, I. H. Chu, C. Chen, Z. Zhu, C. Zheng and S. P. Ong, *Chem. Mater.*, 2018, **30**, 163–173.
6 M. D. Ediger and P. Harrowell, *J. Chem. Phys.*, 2012, 137, 080901.
7 L. Porz, T. Swamy, B. W. Sheldon, D. Rettenwander, T. Frömling, H. L. Thaman, S. Berendts, R. Uecker, W. C. Carter and Y.-M. M. Chiang, *Adv. Energy Mater.*, 2017, **7**, 1701003.
8 C. Ma, K. Chen, C. Liang, C. W. Nan, R. Ishikawa, K. More and M. Chi, *Energy Environ. Sci.*, 2014, **7**, 1638–1642.
9 A. Hein, J. Martin, M. Schäfer and K. M. Weitzel, *J. Phys. Chem. C*, 2017, **121**, 3203–3211.
10 J. B. Bates, N. J. Dudney, G. R. Gruzalski, R. A. Zuhr, a. Choudhury, C. F. Luck and J. D. Robertson, *Solid State Ionics*, 1992, **53**–**56**, 647–654.
11 J. Li, C. Ma, M. Chi, C. Liang and N. J. Dudney, *Adv. Energy Mater.*, 2015, **5**, 1401408.
12 E. G. Herbert, W. E. Tenhaeff, N. J. Dudney and G. M. Pharr, *Thin Solid Films*, 2011, **520**, 413–418.
13 Y. Zhu, X. He and Y. Mo, *ACS Appl. Mater. Interfaces*, 2015, **7**, 23685–23693.
14 A. Schwöbel, R. Hausbrand and W. Jaegermann, *Solid State Ionics*, 2015, **273**, 51–54.
15 K. Leung, A. J. Pearse, A. A. Talin, E. J. Fuller, G. W. Rubloff and N. A. Modine, *ChemSusChem*, 2018, **11**, 1956–1969.
16 V. Lacivita, A. S. Westover, A. Kercher, N. D. Phillip, G. Yang, G. Veith, G. Ceder and N. J. Dudney, *J. Am. Chem. Soc.*, 2018, **140**, 11029–11038.
17 F. Mũnoz, *J. Power Sources*, 2012, 198, 432–433.
18 S. Sicolo and K. Albe, *J. Power Sources*, 2016, **331**, 382–390.
19 S. Sicolo, M. Fingerle, R. Hausbrand and K. Albe, *J. Power Sources*, 2017, **354**, 124–133.
20 Z. Hu, D. Li and K. Xie, *Bull. Mater. Sci.*, 2008, **31**, 681–686.
21 É. Guille, G. Vallverdu, Y. Tison, D. Bégué and I. Baraille, *J. Phys. Chem. C*, 2015, **119**, 23379–23387.
22 V. Lacivita, N. Artrith and G. Ceder, *Chem. Mater.*, 2018, **30**, 7077–7090.
23 T. M. Alam and R. K. Brow, *J. Non. Cryst. Solids*, 1998, **223**, 1–20.
24 F. Muñoz, L. Delevoye, L. Montagne and T. Charpentier, *J. Non. Cryst. Solids*, 2013, **363**, 134–139.
25 P. E. Stallworth, F. Vereda, S. G. Greenbaum, T. E. Haas, P. Zerigian and R. B. Goldner, *J. Electrochem. Soc.*, 2005, **152**, A516.
26 N. Mascaraque, A. Durán, F. Muñoz and G. Tricot, *Int. J. Appl. Glas. Sci.*, 2016, **7**, 69–79.
27 R. K. Brow, *J. Non. Cryst. Solids*, 2000, 263–264, 1–28.
28 B. Raguž, K. Wittich and R. Glaum, *Eur. J. Inorg. Chem.*, 2019, **2019**, 1688–1696.
29 T. M. Alam and R. K. Brow, *NMR studies of bond arrangements in alkali phosphate glasses*, 1998.
30 B. C. Bunker, D. R. Tallant, C. A. Balfe, R. J. Kirkpatrick, G. L. Turner and M. R. Reidmeyer, *J. Am. Ceram. Soc.*, 1987, **70**, 675–681.
31 F. Muñoz, A. Durán, L. Pascual, L. Montagne, B. Revel and A. C. M. Rodrigues, *Solid State Ionics*, 2008, **179**, 574–579.
32 L. Le Van-Jodin, F. Ducroquet, F. Sabary and I. Chevalier, *Solid State Ionics*, 2013, **253**, 151–156.
33 C. J. Pickard and F. Mauri, *Phys. Rev. B - Condens. Matter Mater. Phys.*, 2001, **63**, 2451011–2451013.
34 L. Martel, A. Kovács, K. Popa, D. Bregiroux and T. Charpentier, *Solid State Nucl. Magn. Reson.*, 2020, **105**, 101638.
35 K. Pilar, Z. Deng, M. B. Preefer, J. A. Cooley, R. Clément, R. Seshadri and A. K. Cheetham, *Phys. Chem. Chem. Phys.*, 2019, **21**, 10070–10074.
36 M. Edén, *Annu. Reports Prog. Chem. - Sect. C*, 2012, 108, 177–221.
37 M. R. Reidmeyer and D. E. Day, *J. Non. Cryst. Solids*, 1995, **181**, 201–214.
38 A. Le Sauze, L. Montagne, G. Palavit and R. Marchand, *J. Non. Cryst. Solids*, 2001, **293**–**295**, 81–86.
39 H. Sun, S. Dwaraknath, H. Ling, X. Qu, P. Huck, K. A. Persson and S. E. Hayes, *npj Comput. Mater.*, 2020, **6**, 1–7.
40 M. Marple, J. Badger, I. Hung, Z. Gan, K. Kovnir and S. Sen, *Angew. Chemie - Int. Ed.*, 2017, **56**, 9777–9781.
41 S. Sakida, S. Hayakawa and T. Yoko, *J. Non. Cryst. Solids*, 1999, **243**, 1–12.
42 B. Wang, B. C. Chakoumakos, B. C. Sales, B. S. Kwak and J. B. Bates, *J. Solid State Chem.*, 1995, **115**, 313–323.
43 I. Hung, T. Edwards, S. Sen and Z. Gan, *J. Magn. Reson.*, 2012, **221**, 103–109.
44 R. Witter, P. Hartmann, J. Vogel and C. Jäger, *Solid State Nucl. Magn. Reson.*, 1998, **13**, 189–200.
45 A. Sepúlveda, F. Criscuolo, B. Put and P. M. Vereecken, *Solid State Ionics*, 2019, **337**, 24–32.
46 M. D. Ediger, *J. Chem. Phys.*, 2017, **147**, 210901.
47 Y. Qiu, M. E. Bieser and M. D. Ediger, *J. Phys. Chem. B*, 2019, **123**, 10124–10130.
48 S. F. Swallen, K. L. Kearns, M. K. Mapes, Y. S. Kim, R. J. McMahon, M. D. Ediger, T. Wu, L. Yu and S. Satija, *Science (80-.).*, 2007, **315**, 353–356.
49 P. Luo, C. R. Cao, F. Zhu, Y. M. Lv, Y. H. Liu, P. Wen, H. Y. Bai, G. Vaughan, M. Di Michiel, B. Ruta and W. H. Wang, *Nat. Commun.*, 2018, **9**, 1–7.
50 K. Zhang, Y. Li, Q. Huang, B. Wang, X. Zheng, Y. Ren and W. Yang, *J. Phys. Chem. B*, 2017, **121**, 8188–8194.
51 Q. Zheng, Y. Zhang, M. Montazerian, O. Gulbiten, J. C. Mauro, E. D. Zanotto and Y. Yue, *Chem. Rev.*, 2019, **119**, 7848–7939.
52 J. Li, N. J. Dudney, J. Nanda and C. Liang, *ACS Appl. Mater. Interfaces*, 2014, **6**, 10083–10088.
53 C. S. S. Nimisha, K. Y. Rao, G. Venkatesh, G. M. Rao and N. Munichandraiah, *Thin Solid Films*, 2011, **519**, 3401–3406.
54 C. Monroe and J. Newman, *J. Electrochem. Soc.*, 2003, **150**, A1377.

10.1002/anie.202009501

WILEY-VCH

RESEARCH ARTICLE

Entry for the Table of Contents

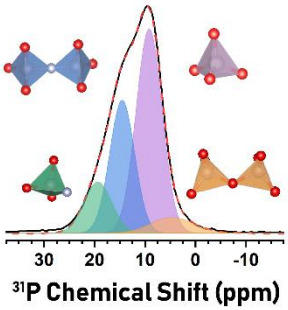

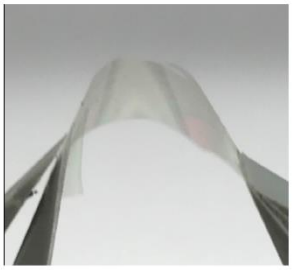

LiPON's local structure: LiPON, known for cyclability against Li metal anodes, is examined using complimentary solid-state NMR and *ab initio* calculations. LiPON is determined to be composed of primarily monomers and dimers with no signs of extended chains. A free-standing film of LiPON suggests the glassy structure is responsible for unique mechanical behavior.